Probing electronic motion and core potential by Coulomb-reshaped terahertz radiation

Ziyang Gan,[1,2,3] Kaixuan Zhang,[1,4] Yuan Gao,[1] Ahai Chen,[2] Yizhu Zhang,[1,5,6,*] Tian-Min Yan,[1,†] Thomas Pfeifer,[6] and Yuhai Jiang[1,2,‡]

[1]*Shanghai Advanced Research Institute, Chinese Academy of Sciences, Shanghai 201210, China*
[2]*Center for Transformative Science, School of Physical Science and Technology, ShanghaiTech University, Shanghai 201210, China*
[3]*University of Chinese Academy of Sciences, Beijing 100049, China*
[4]*Zhejiang Provincial Key Laboratory of Ultra-Weak Magnetic-Field Space and Applied Technology, Hangzhou Innovation Institute, Beihang University, Hangzhou 310051, China*
[5]*Center for Terahertz Waves and College of Precision Instrument and Optoelectronics Engineering, Key Laboratory of Opto-electronics Information and Technical Science, Ministry of Education, Tianjin University, Tianjin 300350, China*
[6]*Max-Planck Institute for Nuclear Physics, Heidelberg 69117, Germany*

(Received 5 June 2023; revised 5 January 2024; accepted 17 June 2024; published 11 July 2024)

The nature of electronic motion and structural information of atoms and molecules is encoded into strong-field-induced radiation ranging from terahertz (THz) to extreme ultraviolet wavelength. The dependence of THz yields in bichromatic laser fields on ellipticity and interpulse phase delay was experimentally measured, and the trajectory calculations establish the link between the THz emission and the motion of the photoelectron wave packet. The interaction between the photoelectron and the parent core transforms from a soft collision to recollision as the laser field is tuned from elliptical to linear polarization, which can be reflected in THz emission. The soft collision is found to be more effective in reconstructing electron dynamics through THz polarization, which enables us to construct the effective core potential of the generating medium with the Coulomb-reshaped THz radiation in an elliptically polarized laser field. Our work enables us to design innovative all-optical THz measurements of electronic and structural dynamics.

DOI: 10.1103/PhysRevA.110.013110

I. INTRODUCTION

Strong-field-induced radiation ranging from terahertz (THz) to extreme ultraviolet wavelength contains a wealth of structural and dynamical information of the generating medium. High-harmonic generation (HHG) of extreme ultraviolet photons has been widely used for molecular orbital tomography [1,2], and the probing of electron wave packets [3,4], nuclear dynamics, and structural rearrangement on a subfemtosecond timescale [5–7]. Analogous to HHG, THz wave generation (TWG) [8], also known as zeroth-order Brunel harmonics [9], has also been considered as an all-optical approach for probing molecular structures [10]. It was recently used as an innovative optical attoclock [11] where the THz polarization direction acts as a "clock hand" for mapping the tunneling delay, laterally complementing the currently used attoclock implemented in photoelectron momentum spectroscopy [12–15].

Strong-field-induced TWG physically originates from the acceleration of a tunneling photoelectron wave packet in an oscillating electric field, described macroscopically by the photocurrent (PC) model [16] or microscopically by a continuum-continuum transition in the strong field approximation [17,18]. In typical scenarios when fitting the macroscopic THz yield, the aforementioned models, neglecting the Coulomb interaction between the free electron and the parent core, suffice. Nevertheless, when employing all-optical THz probing to investigate microscopic structures and electron dynamics, the Coulomb effect becomes highly sensitive and thus necessitates careful consideration.

The Coulomb influence on photoelectron momentum spectra and HHGs, when retrieving the photoelectron dynamics, has been very apparent. When measuring the electron tunneling delay implemented by the attoclock [13–15], all those works emphasized that the Coulomb interaction must be taken into account, and the tunneling delay has to be correctly disentangled from the final photoelectron momentum spectra to achieve a meaningful quantitative interpretation. The Coulomb-reshaped electronic wave packet has been encoded in the phase of HHGs [19], which affects the accuracy of structural tomography [2,20,21]. For TWGs, the involvement of the Coulomb potential in microscopic information extraction, as well as the speculation on photoelectron motion and structural information, has been rarely investigated.

Although the TWG has been well described by the PC model [16,22], where the net residual photocurrent density plays the core role, the photocurrent lacks more fine-grained microscopic information of photoelectron dynamics. As the photocurrent is essentially a macroscopic correspondence of an asymmetric photoelectron wave packet conceptually described by an ensemble of propagating photoelectron trajectories [23,24], the TWG can be evaluated from microscopic trajectories to account for the influence from both the external

*Contact author: zhangyizhu@tju.edu.cn
†Contact author: yantm@sari.ac.cn
‡Contact author: jiangyh3@shanghaitech.edu.cn

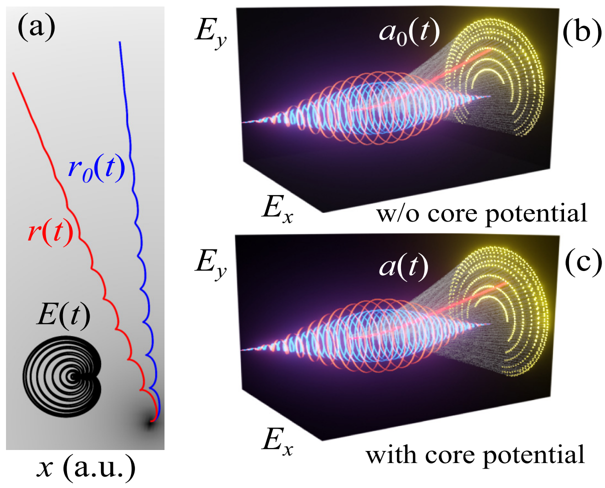

FIG. 1. The influence of Coulomb interaction on photoelectron trajectories. Panel (a) shows an exemplary trajectory of a photoelectron, either subjected to the Coulomb potential (red) or not (blue). Panels (b) and (c) show the distribution of a photoelectron wave packet as an ensemble of classical trajectories with and without Coulomb interaction as indicated.

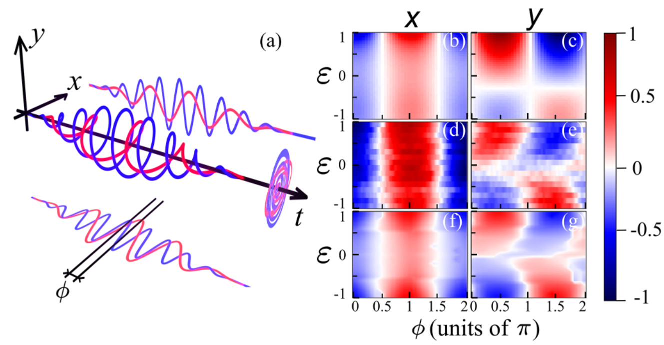

FIG. 2. The THz peak-to-peak distributions in two-color fields $S_{\mathrm{pp},\sigma}(\varepsilon,\phi)$. Panel (a) presents an illustration of the laser fields, where the ω-field (red) is elliptically polarized with an ellipticity ε and the 2ω-field (blue) is circularly polarized. The $\omega-2\omega$ phase delay is ϕ. The x direction is defined as parallel to the polarization of the ω-field when $\varepsilon=0$ (see Appendix A for a detailed definition). The PP distributions in the x direction, $S_{\mathrm{pp},x}(\varepsilon,\phi)$, are shown for (b) the PC model, (d) experiment, and (f) CTMC. Correspondingly, the PP distributions in the y direction, $S_{\mathrm{pp},y}(\varepsilon,\phi)$, are shown in panels (c), (e), and (g).

field $\boldsymbol{E}(t)$ and the potential of the parent ion $V(\boldsymbol{r})$ [25]. This influence is experimentally substantiated by measuring the optimal THz yields as a function of two-color phase delay [25], as well as by examining the THz polarization under specific polarization combinations of two-color fields [26].

In this work, according to the classical trajectory Monte Carlo (CTMC) method, we elucidate how various types of electron-core interactions, including soft collisions and recollisions, are imprinted in the TWG polarization. Meanwhile, it reveals the equivalence between the THz polarization and the asymmetry pointer of photoelectron momentum distributions (PMDs), which can be substantially employed for the reconstruction of atomic core potentials.

II. COULOMB EFFECT ON THz WAVE EMISSION

In the CTMC method, within an ensemble of trajectories $\{i\}$, the ith trajectory $\boldsymbol{r}_i(t)$ is determined by solving the equation of motion $\boldsymbol{a}_i(t)\equiv\partial^2\boldsymbol{r}_i(t)/\partial t^2=-\boldsymbol{E}(t)-\nabla V[\boldsymbol{r}_i(t)]$ starting from the initial tunneling time $t_0^{(i)}$. The initial conditions and ionization rate w_i of the CTMC method are detailed in Appendix B. The radiation derives from the acceleration of the ensemble $\boldsymbol{a}(t)=\sum_i w_i\Theta(t-t_0^{(i)})\boldsymbol{a}_i(t)$, with $\Theta(t)$ the Heaviside function [27,28]. The time-domain THz wave is obtained by evaluating $\mathscr{F}^{-1}\{\mathscr{W}\mathscr{F}\{\boldsymbol{a}(t)\}(\omega)\}(t)$, with $\mathscr{F}$ the Fourier transform and $\mathscr{W}$ the low-pass filter. Taking the two-color bi-circularly-polarized fields, for instance, once the electron is released from the atom, its trajectory, compared to the path $\mathbf{r}_0(t)$ driven solely by the external light field, may become a bent one $\mathbf{r}(t)$ in the presence of Coulomb interaction, as shown in Fig. 1(a).

The Coulomb effects on each trajectory eventually alter the global distribution of the electronic wave packet. Figure 1(b) shows the ensemble of trajectories when the Coulomb potential is absent. At an arbitrary time t, the positions of all classical trajectories, $r_0^{(i)}(t)$, correspond to the spatial distribution of the photoelectron wave packet. The radiation is induced by the ensemble acceleration $\langle\boldsymbol{a}_0(t)\rangle=-\boldsymbol{E}(t)n(t)$, showing a consistent form to the PC model [16], but with the electron density $n(t)=\sum_i w_i\Theta(t-t_0^{(i)})$ as a sum over all trajectories. When the parent ion is present, the distribution of trajectories is slightly distorted, as shown in Fig. 1(c). The distortion may result in observable patterns in PMD, and also equips the acceleration with a correction term, $\langle\boldsymbol{a}(t)\rangle=\langle\boldsymbol{a}_0(t)\rangle+\langle\boldsymbol{a}_C(t)\rangle$, with $\langle\boldsymbol{a}_C(t)\rangle=\sum_i w_i\Theta(t-t_0^{(i)})\frac{\boldsymbol{r}_i(t)}{|\boldsymbol{r}_i^3(t)|}$ from the Coulomb potential, inducing extra modulation in radiation.

We explore TWG in two-color fields by mixing the fundamental of a Ti:sapphire laser [800 nm (ω), 35 fs] with its second harmonic [400 nm (2ω), circularly polarized]. The ω and 2ω beams have intensities of $I=1.5\times10^{14}$ W/cm^2 and $I/2$, respectively. As schematically demonstrated in Fig. 2(a), we measure the THz yield $S(\varepsilon,\phi)$ as a function of ε, the ellipticity of the ω beam, and ϕ, the interpulse phase delay. The TWGs are detected with electro-optic sampling, and the polarization components of time-domain waveform $E_{\mathrm{THz},\sigma}(t)$ $(\sigma\equiv x,y)$ are recorded. Defining the THz peak-to-peak (PP) amplitude, $S_{\mathrm{pp},\sigma}=\pm|\max[E_{\mathrm{THz},\sigma}(t)]-\min[E_{\mathrm{THz},\sigma}(t)]|$, we measure the dependence of $S_{\mathrm{pp},\sigma}$ on $\varepsilon\in[0,\ 1]$ and $\phi\in[0,\ 2\pi]$. As the absolute time zero of ϕ is technically challenging to determine in the experiment, we further propose a method based on CTMC to determine ϕ by measuring TWG polarization directions (see the subsequent parts). A detailed experimental setup, raw data, and the self-referencing method are presented in Appendix A.

Figures 2(b)–2(g) present the distributions of $S_{\mathrm{pp},\sigma}(\varepsilon,\phi)$ obtained from the PC model, experiment, and the CTMC method. Contrary to the distribution of $S_{\mathrm{pp},y}(\varepsilon,\phi)$ evaluated by the PC model shown in Fig. 2(c), the experimental result in (e) exhibits a bend along ε, which can be replicated by the CTMC calculation in panel (g). The CTMC calculations without Coulomb potential show the same results as the PC model, confirming the equivalence between the two methods.

Thus, the bend by comparison shown in Fig. 2 is confirmed to be attributed to the Coulomb effects. The bend of $S_{\mathrm{pp,y}}$ induced by the Coulomb potential is more pronounced than that of $S_{\mathrm{pp,x}}$, because, along the y direction, the contribution of the Coulomb potential to the photoelectron momentum is comparable to the momentum induced by the laser field.

Through CTMC, the TWG is closely tied to the photoelectron wave packet as an ensemble of trajectories. The CTMC model establishes a correlation between the TWGs and PMDs. The THz emission ($\boldsymbol{E}_{\mathrm{THz}}$) from the trajectory ensemble is expressed as the summation of individual trajectories as

$$\boldsymbol{E}_{\mathrm{THz}}(\omega \to 0) = \sum_i w_i \left(\lim_{\omega \to 0} \int_{-\infty}^{\infty} dt \frac{\partial \boldsymbol{v}_i(t)}{\partial t} e^{-i\omega t} \right) = \sum_i w_i \boldsymbol{v}_i(\infty). \quad (1)$$

Here, ω represents the frequency of strong-field-induced radiation, and $\boldsymbol{v}_i(t)$ and $\boldsymbol{v}_i(\infty)$ denote the instantaneous velocity and asymptotic velocity (drift velocity) of the ith trajectory. The contribution of the ith trajectory to TWG is expressed as $\boldsymbol{E}_{\mathrm{THz},i} \propto w_i \boldsymbol{v}_i(\infty)$. The polarization direction of $\boldsymbol{E}_{\mathrm{THz},i}$ is defined as $\hat{\boldsymbol{E}}_{\mathrm{THz},i}$, equivalent to the direction of asymptotic velocity $\hat{\boldsymbol{v}}_i(\infty)$. The amplitude of $\boldsymbol{E}_{\mathrm{THz},i}$ is defined as $|\boldsymbol{E}_{\mathrm{THz},i}| \propto |w_i \boldsymbol{v}_i(\infty)|$. We define the asymmetry of PMDs as $\mathbf{P}_e = \sum_i w_i \boldsymbol{v}_i(\infty)$ with an asymmetrical direction of $\hat{\mathbf{P}}_e$. $\boldsymbol{E}_{\mathrm{THz}}$ is proportional to $\mathbf{P}_e$, which is equivalent to the residual photocurrent in the PC model.

In Figs. 3(a)–3(d), we present $\hat{\boldsymbol{E}}_{\mathrm{THz},i}$ and $|\boldsymbol{E}_{\mathrm{THz},i}|$ of the highest-weight trajectories with respect to ε and ionization instants t_0 for two selected $\phi = 0, \pi/2$. Figures 3(e)–3(h) analyze the TWGs from the trajectory ensemble, where the calculated $\hat{\boldsymbol{E}}_{\mathrm{THz}}$, $\hat{\mathbf{P}}_e$, and measured THz polarization θ_{THz} are depicted in direct comparison with PMDs at $\varepsilon = 0, 1$. The corresponding simulation results of $\hat{\boldsymbol{E}}_{\mathrm{THz},i}$, $|\boldsymbol{E}_{\mathrm{THz},i}|$, $\hat{\boldsymbol{E}}_{\mathrm{THz}}$, $\hat{\mathbf{P}}_e$, and PMDs without Coulomb potential are shown in Fig. 7 of Appendix B for comparison.

For large ellipticities $\varepsilon > 0.4$, Figs. 3(a) and 3(b) illustrate that $\hat{\boldsymbol{E}}_{\mathrm{THz},i}$ smoothly changes with respect to t_0. In Figs. 3(c) and 3(d), the maxima of $|\boldsymbol{E}_{\mathrm{THz},i}|$ correspond to the peak values of the two-color fields (dashed lines), where the tunneling ionization rate reaches its maximum. These maxima represent the main tunneling temporal windows. Figures 3(e) and 3(g) for $\varepsilon = 1$ exhibit that $\hat{\boldsymbol{E}}_{\mathrm{THz}}$ (black solid lines) coincides with $\hat{\mathbf{P}}_e$ (red solid lines), as predicted in Eq. (1). The angular deviations observed between $\hat{\boldsymbol{E}}_{\mathrm{THz}}$ with (black solid lines) and without (green solid lines) Coulomb potential result from the deflection of electron trajectory induced by the Coulomb potential, i.e., soft collision between the electron and the parent ion. The angular deviation corresponds to the "streaking angle" in the "attoclock" of PMDs [11].

As ε decreases, chaos regions and gray regions emerge, highlighted in the red boxes in Figs. 3(a) and 3(b). The gray regions are explained by the scenario in which the parent core recaptures the free electron in the Rydberg state. The chaotic regions arise from the hard recollision between the electron and the parent core, resulting in the emission of $\hat{\boldsymbol{E}}_{\mathrm{THz},i}$ occurring near-isotropically across all 4π solid angles. Trajectories within chaos regions that do not overlap with the maximum

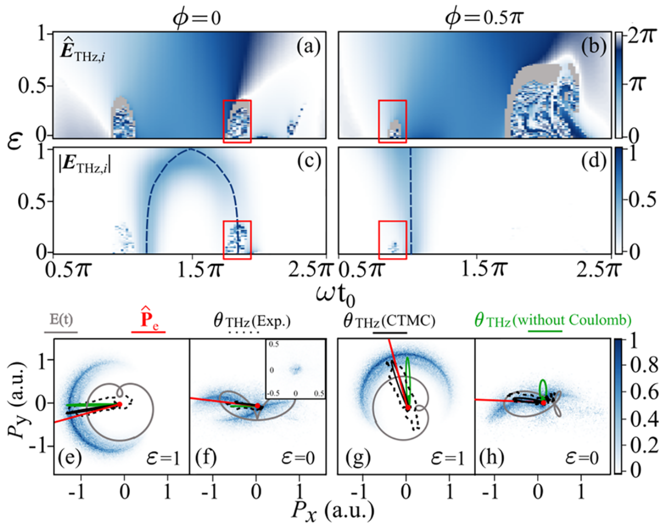

FIG. 3. The trajectory analysis of THz emissions at various ellipticities ε for two selected phase delays $\phi = 0, \pi/2$. (a)–(d) Contribution of the ith individual trajectory to THz emission $\boldsymbol{E}_{\mathrm{THz},i}$ with respect to ε and ionization instants t_0. Panels (a) and (c) show the polarization direction $\hat{\boldsymbol{E}}_{\mathrm{THz},i}$ and the amplitude $|\boldsymbol{E}_{\mathrm{THz},i}|$ at $\phi = 0$. Panels (b) and (d) show $\hat{\boldsymbol{E}}_{\mathrm{THz},i}$ and $|\boldsymbol{E}_{\mathrm{THz},i}|$ at $\phi = \pi/2$. (e)–(h) THz emissions from the trajectory ensemble $\boldsymbol{E}_{\mathrm{THz}}$. The PMDs, laser electric fields (gray bold lines), THz polarization $\hat{\boldsymbol{E}}_{\mathrm{THz}}$ with (black solid lines) or without (green solid lines) Coulomb potential, asymmetry pointer of PMDs $\hat{\mathbf{P}}_e$ (red solid lines), and the experimental THz polarization θ_{THz} (dashed lines) are presented for comparison. The inset in panel (f) depicts the PMD of selected trajectories in the red box in panels (a) and (c).

region of $|\boldsymbol{E}_{\mathrm{THz},i}|$, as depicted in Figs. 3(b) and 3(d), contribute minimally to TWGs due to their low weight. However, when the chaos region overlaps with the right branch of tunneling windows, shown as red boxes in panels (a) and (c), the recollision trajectories significantly influence the TWGs. The isotropic distribution of $\hat{\boldsymbol{E}}_{\mathrm{THz},i}$, as shown in the inset of panel (f), leads to the counterbalancing of contributions from individual trajectories. In Fig. 3(f), the angular deviations between $\hat{\boldsymbol{E}}_{\mathrm{THz}}$ with and without Coulomb potential cannot be observed as in the case of $\varepsilon = 1$. This can be explained by the scenario that, although $\hat{\boldsymbol{E}}_{\mathrm{THz},i}$ are deflected by the Coulomb potential, the high-weight trajectories within the right branch of the tunneling windows do not contribute to the TWGs, thus the Coulomb potential is not effectively manifest in the TWGs.

When ε changes from 1 to 0, the electron-core interaction transitions from a soft collision to a hard recollision, manifested in the ϕ-dependent TWGs. In a hard recollision, the random scattering breaks the homogeneous behavior of the trajectory ensemble, diminishing the effectiveness of the encoding dynamics and the structural information in the TWGs. In contrast, during a soft collision, the Coulomb potential deflects the trajectory ensemble while maintaining its homogeneous behavior. In this scenario, the trajectory ensemble can be approximately represented by the highest-weight trajectory, providing a more straightforward basis for reconstructing the electron dynamics. This analysis can be further simplified by an analytical solution obtained through perturbatively evaluating the Coulomb-induced correction to the guiding center trajectory, where the fast timescale laser-induced oscillation is averaged out [29]. Refer to Eqs. (D5), (D6), and (D15) in Appendix D for more details.

III. RECONSTRUCTION OF POTENTIAL BY THz RADIATION

The all-optical reconstruction of the core potential of the generating medium is conceptually straightforward. If a sufficiently broad spectrum of the radiated field, $\tilde{\boldsymbol{E}}_{\rm rad}(\omega)$, can be acquired, the reconstructed acceleration of a photoelectron, $\boldsymbol{a}(t) = \boldsymbol{E}_{\rm rad}(t)$, in principle, enables us to trace the local potential, $\nabla V(\boldsymbol{r}) = -\boldsymbol{a}_C(\boldsymbol{r}(t)) = -[\boldsymbol{a}(t) + \boldsymbol{a}_{\boldsymbol{0}}(t)]$. Multiple trajectories under a different phase delay ϕ, therefore, sketch the contour of $\nabla V(\boldsymbol{r})$ as analogous to the mesh representation of an object in an artistic wire sculpture (see Appendix E for details).

The acceleration $\boldsymbol{a}_C$ induced by the Coulomb potential becomes significant only when the electron-nucleus distance $\boldsymbol{r}(t)$ is very small. Consequently, the Coulomb potential seriously modifies the TWG during the initial phase when the electron has just departed from the core after ionization. The TWG modification within a narrow temporal window corresponds to the high-frequency component of THz emissions. Theoretical testing suggests that the accurate reconstruction of the entire profile of the Coulomb potential would necessitate a broad-spectrum THz coverage up to 280 THz. However, despite recent significant advancements in generating and detecting broadband THz emissions in gas plasma, the capabilities of TWG generation and detection remain restricted to 100 THz. The practical limitation in our setup allows for reliable measurement only from 0.1 to 3 THz. Fortunately, the TWG is determined by the slow timescale dynamics that are highly sensitive to the initial stage of the photoelectron motion. As the interaction with the parent ion can dramatically alter the photoelectron trajectory when the electron roams around the core within a short time after the tunneling ionization, it is hence still possible to extract partial information by exploiting the TWG.

This can be shown by an example in which a key parameter of the effective potential is retrieved. We assume a Coulomb potential $V(\boldsymbol{r}) = -\frac{Z_{\rm eff}}{|\boldsymbol{r}|}$, with $Z_{\rm eff}$ the effective charge, which reflects the strength of the Coulomb potential, to be determined. The polarization direction of TWG as a function of phase delay ϕ, i.e., $\theta_{\rm THz}(\phi)$, can be experimentally measured by scanning ϕ. The absolute ϕ can be determined by comparing the measurement and theories, including CTMC and direct solution of the time-dependent Schrödinger equation (TDSE). As shown in Fig. 4(a), $\theta_{\rm THz} = 0^\circ, 180^\circ$ at $\phi = 0^\circ, 180^\circ$ remains identical regardless of $Z_{\rm eff}$, establishing a criterion for determining the absolute ϕ (see Appendix E for a detailed calibration).

As shown in Fig. 4(a), $\theta_{\rm THz}(\phi)$ possesses a high correlation with $Z_{\rm eff}$, allowing for the determination of $Z_{\rm eff}$ by comparing the experimentally obtained $\theta_{\rm THz}(\phi)$ with that from the simulation. Figures 4(b) and 4(c) present the same plots as Figs. 3(e)–3(h) for $\varepsilon = 0.4$, $\phi = 0, \pi/2$ as a further inspection of the comparison of TWG polarization and angular streaking in PMDs. The $\theta_{\rm THz}(\phi)$ in our measurement and the emitting angle in the "phase-of-phase (POP) attoclock" experiment [30] show similar evolution with respect to ϕ. Considering the connection between TWGs and PMDs mentioned above, it validates the reconstruction methodology based on TWGs and provides a potential avenue for extracting tunneling ionization dynamics in future studies as an alternative to the "POP attoclock."

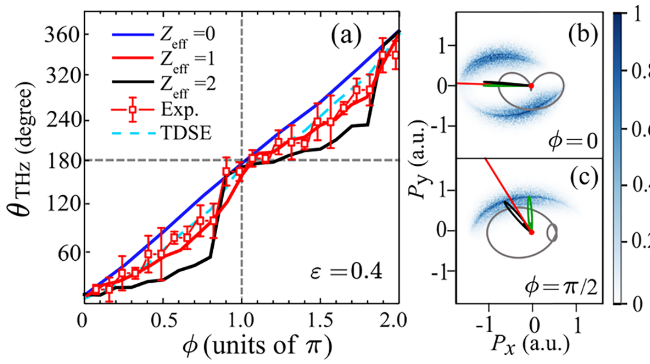

FIG. 4. Reconstruction for the effective Coulomb potential with THz polarizations. (a) Dependence of the THz polarization direction $\theta_{\rm THz}(\phi)$ on time delay ϕ with different effective charge $Z_{\rm eff}$ at $\varepsilon = 0.4$. (b) and (c) The same plots as Figs. 3(e)–3(h), but for $\varepsilon = 0.4$, $Z_{\rm eff} = 1$ at $\phi = 0$ and $\pi/2$, respectively.

IV. CONCLUSION

In this work, we found that the dependence of THz yields on the ellipticity and interpulse phase delay of a bichromatic laser cannot be explained by the PC model due to the absence of the photoelectron-core interaction. The inclusion of the Coulomb potential in the CTMC model not only reproduces the experimental results, but it also establishes the connection between THz radiation and photoelectron motion. Compared to the recollision scenario at low ellipticity, the structure information is more efficiently encoded in the motion of a trajectory ensemble after a soft collision at intermediate ellipticity. Therefore, with the support of CTMC and TDSE simulation, we introduce a reconstruction methodology for extracting the local potential by measuring THz polarizations with respect to the two-color phase delay. The THz polarization is equivalent to the asymmetry pointer of PMDs, connecting our measurement and "attoclock" of PMDs. In contrast to the angular offset in the conventional "attoclock," our experiment allows for a precise and easy-to-implement determination of THz polarization. Furthermore, TWGs emitted from condensed-phase media provide an opportunity to extract electron motion and structure in the bulk solid or liquid targets.

ACKNOWLEDGMENTS

This work was supported by the National Key Research and Development Program of China (Grants No. 2022YFA1604302) and the National Natural Science Foundation of China (Grants No. 12334011, No. 12174284, and No. 12374262). We acknowledge the computational resources of the HPC platform in ShanghaiTech University.

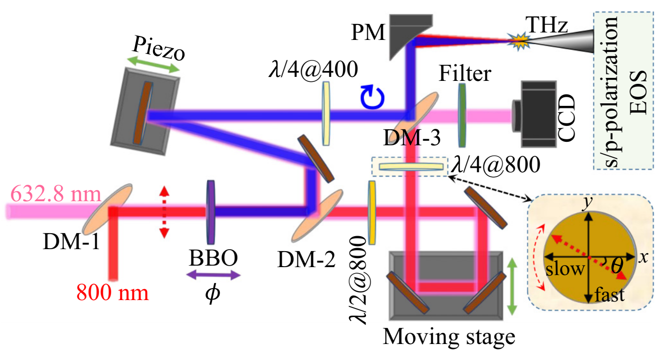

FIG. 5. Schematic illustration of the experimental setup. DM: dichroic mirror; BBO, beta barium borate; PM, parabolic mirror; $\lambda/4$ and $\lambda/2$, quarter-wave plate and half-wave plate. A phase stabilization module based on a Mach-Zehnder interferometer is used to eliminate the phase jitter between the two-color pulses. The ellipticity of an 800 nm pulse is adjusted from -1 to 1, and the 400 nm pulse is circularly polarized. The x- or y-polarized THz waveforms can be detected by free-space polarization-sensitive electro-optic sampling.

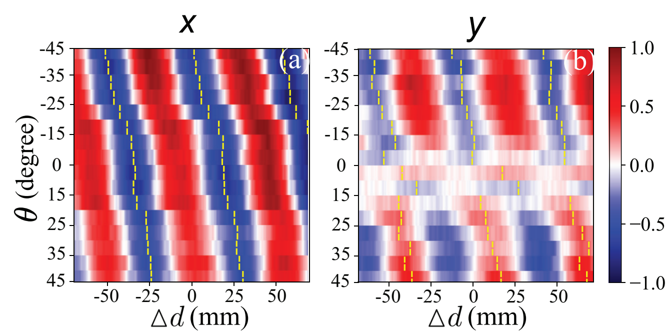

FIG. 6. Row data of THz yield measurements. (a) and (b) x- and y-polarized THz electric field peak-to-peak amplitudes as a function of the polarization orientation of 800 nm fields θ and the BBO positions d represented by $S_x(d,\theta)$ and $S_y(d,\theta)$. After data processing, they are realigned and converted into the THz yields as a function of ω–2ω phase delays ϕ and the ellipticity of 800 nm electric fields ε [$S_x(\phi,\varepsilon)$ and $S_y(\phi,\varepsilon)$ in Fig. 2 in. the main text].

APPENDIX A: EXPERIMENT AND DATA PROCESSING

The experimental setup is illustrated in Fig. 5. Horizontally polarized (x-polarized) fundamental pulses with a repetition of 1 kHz, a center wavelength of 800 nm, a pulse duration of 35 fs, and a pulse energy of 2 mJ are delivered by a Ti:sapphire amplifier. After passing through a 200-μm type-I beta barium borate (β-BBO) crystal with a double-frequency efficiency of ∼30%, the two-color ($\omega - 2\omega$) laser pulses are then split into two independent paths by a dichroic mirror (DM). In the 2ω path, the 400 nm laser is fixed to be circularly polarized by appropriately adjusting the quarter-wave plate ($\lambda/4$@400 nm). In the ω path, as shown in the inset, the optical slow axis of the quarter-wave plate ($\lambda/4$@800 nm) is fixed along the horizontal direction (x axis). By rotating the half-wave plate ($\lambda/2$@800 nm) to change the angle θ between the polarization direction of the ω beam and the optical slow axis of the quarter-wave plate from -45° to 45°, thus the ellipticity ε of the ω beam can be regulated from -1 to 1. Finally, the separated paths of the $\omega - 2\omega$ beam are combined by another dichroic mirror and then focused by a 100-mm focus-length off-axis parabolic mirror to ionize the ambient air and generate terahertz (THz) radiation.

When implementing the experiment, the variation of the $\omega - 2\omega$ phase delay ϕ can be achieved by changing the position d of the BBO crystal. Specifically, due to the difference of the $\omega - 2\omega$ refractive indices in the air, moving BBO forwards or backwards a distance of ∼5.5 cm along the propagation direction corresponds a phase delay of 2π of an 800 nm electric field. Note that in order to eliminate the relative phase jitter between the ω-2ω pulses mainly caused by mechanical vibration and airflow, a phase-stabilization module based on a Mach-Zehnder interferometer is adopted [31]. In this module, a mirror fixed on a piezoelectric transducer is employed to compensate for the phase jitter, and ϕ is stabilized by actively locking the phase of the interference fringes, which is formed by a He-Ne laser of 632.8 nm and detected by a CCD camera. The horizontal and vertical polarized components of THz temporal waveforms are measured by polarization-sensitive free-space electro-optic sampling [32]. S_x and S_y are x- and y-polarized THz peak-peak amplitudes, which can be obtained from the THz waveforms.

In a data-acquisition procedure, ε of the 800 nm beam can be scanned by changing the polarization orientation of 800 nm polarization represented by θ. At each θ, corresponding to different ε, the BBO position d is moved along the propagation direction to scan the ϕ, and S_x and S_y are recorded as a function of d. When θ is changed by rotating the half-wave plate ($\lambda/2$@800 nm), the minor phase drift between the two paths of a Mach-Zehnder interferometer is introduced, which leads to the phase shift of periodic THz yields $S(d)$ at different θ, as shown in Fig. 6. Comparing Figs. 6(a) and 6(b), the phase shift of S_x continuously evolves along the θ axis, whereas the S_y phase evolution is apparently distorted close to $\theta = 0$. To straightforwardly compare $S(\phi)$ at different ε, we realign and convert $S(d,\theta)$ to $S(\phi,\varepsilon)$ with a self-referencing method, where $S_y(\phi)$ is calibrated regarding $S_x(\phi)$ as a reference. At any θ, we realign $S_x(d,\theta)$ by translating $S_x(d,\theta)$ along the d axis by an offset $\Delta d(\theta)$ to fix its maximum at $\phi = \pi$, and then the translation of the same magnitude $\Delta d(\theta)$ is correspondingly implemented on $S_y(d,\theta)$. The procedure is repeated at each θ. The realigned result is plotted in Fig. 2 in the main text.

APPENDIX B: NUMERICAL ANALYSIS WITHOUT COULOMB POTENTIAL

In this Appendix, we will present the emission angles of photoelectron, THz yield, polarization, and photoelectron momentum distribution (PMD) in the absence of the Coulomb potential. By comparing these results with those in Fig. 3 in the main text, we aim to analyze the influence of the Coulomb potential under different conditions. The content presented in Fig. 7 aligns with Fig. 3 in the main text but without the Coulomb potential. As shown in Figs. 3(a)–3(d), in the absence of the Coulomb potential, regardless of the variations in ellipticity and phase difference, the emission angles of photoelectrons and THz yield do not exhibit any peculiar regions caused by rescattering. Therefore, in the absence of

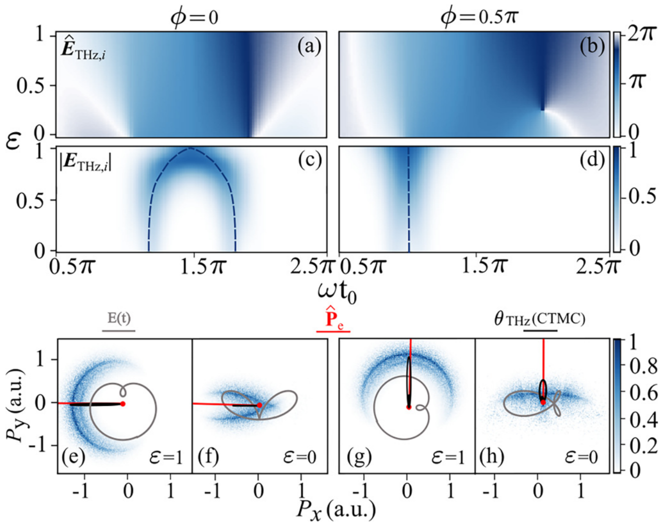

FIG. 7. The CTMC analysis of TWG at different laser ellipticities. The emitting angle of the most probable trajectory released at different times (top panels) and the related TWG yields (middle panels) are presented for $\phi = 0$ and $\pi/2$ as indicated. The bottom panels show comparisons of θ_{THz} with (black solid lines) and without Coulomb potential, and $\hat{\mathbf{P}}_e$ (red solid lines), for $\varepsilon = 1$ and 0 as indicated. The PMD and the laser field (gray bold lines) are also shown for reference.

rescattering and distortion caused by the Coulomb potential, as illustrated in Figs. 3(e)–3(h), the THz polarization direction aligns perfectly with the asymmetry direction of PMD. Taking $\varepsilon = 0$ as an example, under small ellipticities, the generated photoelectrons concentrate at the two peaks of the electric field at $\phi = 0$. Comparing with Figs. 3(a) and 3(c) in the main text, the photoelectron emission angles due to ionization at the left peak are slightly distorted by the Coulomb potential, causing a small deviation around π. However, at the right peak, the scattering effects induced by the Coulomb potential offset each other, resulting in the THz polarization direction in Fig. 3(f) in the main text aligning closely with the photoelectron emission angle at the left peak. When $\phi = 0$, $\varepsilon = 0$, the generated photoelectrons for THz emission concentrate at a single peak of the electric field. Furthermore, due to the distortion induced by the Coulomb potential, the emission angle, originally at $\pi/2$, shifts to π. This ultimately results in the change of THz polarization from Fig. 7(h) to Fig. 3(h) in the main text.

APPENDIX C: TRAJECTORY ANALYSIS WITH COULOMB POTENTIAL

The TWG polarization direction points to the asymptotic direction of the photoelectron trajectory since $\boldsymbol{E}_{\mathrm{THz}} = \lim_{\omega\to 0}\int_{-\infty}^{\infty} dt\, \boldsymbol{a}(t)\, e^{-i\omega t} = \boldsymbol{v}(\infty)$. Thus, the TWG is closely tied to the photoelectron wave packet as an ensemble of trajectories. The asymmetry of the asymptotic photoelectron wave packet is equivalent to the residual photocurrent in the PC model, which is the origin of net THz yield. Hence, the orientation of the asymmetrical distribution of the photoelectron wave packet determines the TWG polarization direction. The wave packets driven by different parameters (ε, ϕ) of

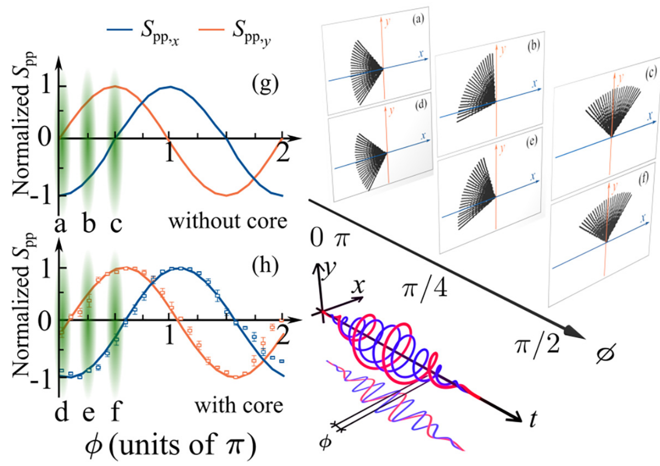

FIG. 8. The THz yields $S_{\mathrm{pp},\sigma}(\varepsilon = 1, \phi)$ and the distributions of a photoelectron wave packet as a function of time delay ϕ in two-color laser fields of $\varepsilon = 1$ as shown in the bottom-right inset. Without Coulomb interaction, the distributions of wave packets as ensembles of classical trajectories are shown in panels (a)–(c), respectively, for $\phi = 0$, $\pi/4$, and $\pi/2$. In comparison, the distributions of the wave packet with Coulomb interaction are shown in (d)–(f). The normalized components of PP values, $S_{\mathrm{pp},\sigma}(\phi)$ $(\sigma = x, y)$, from the experiment (square symbol with error bar) and trajectory-based calculation (solid line), are presented in (g) and (h) for the THz emission without and with Coulomb interaction. The shaded regions, as labeled from "a" to "f," correspond to the wave packets in panels (a)–(f) . The colors of the axes in panels (a)–(f) agree with that of components $S_{\mathrm{pp},x}(\phi)$ (blue) and $S_{\mathrm{pp},y}(\phi)$ (orange) in panels (g) and (h) for visual convenience.

the external fields are subjected to the different Coulomb interaction, affecting the TWG process by means of altering the distribution of the photoelectron wave packet.

When $\varepsilon = 1$, Figs. 8(a)–8(c) show the fanlike wave-packet distributions with their directions changing with ϕ. When the Coulomb interaction is present, the distributions remain fanlike, as shown in Figs. 8(d)–8(f), while their pointing directions are slightly changed, reassigning the TWG polarizations. As shown in Fig. 8(h), both $S_{\mathrm{pp},x}(\phi)$ and $S_{\mathrm{pp},y}(\phi)$ are shifted along ϕ when the Coulomb interaction is present. It is noteworthy that, $S_{\mathrm{pp},y}(\phi)$ being coordinated with $S_{\mathrm{pp},x}(\phi)$, the calibration of $S_{\mathrm{pp},x}(\phi)$ results in the concurrent shift of $S_{\mathrm{pp},y}(\phi)$. Therefore, the distribution of $S_{\mathrm{pp},y}(\phi)$ relative to $S_{\mathrm{pp},x}(\phi)$ with the Coulomb effect, as shown by Fig. 8(h), is roughly the same as that of Fig. 8(g) without the Coulomb effect.

When $\varepsilon = 0$, the wave-packet distribution is dramatically altered by the change of ϕ as shown in Figs. 9(a)–9(f). It appears from a scissorlike distribution at $\phi = 0$ towards the single-branch distribution at $\phi = \pi/4$ and finally reaches a fan-shaped distribution when $\phi = \pi/2$. The Coulomb interaction also rotates the global distribution counterclockwise with increasing ϕ, but the deformation of wave-packet distribution dominates the change of the asymmetry. When $\phi = 0$, there are two peaks of electric field in each cycle where the photoelectron mainly emits, inducing the bifurcation of the wave-packet distribution as shown in Fig. 9(a). Both branches are almost located in the negative x half-plane, causing the

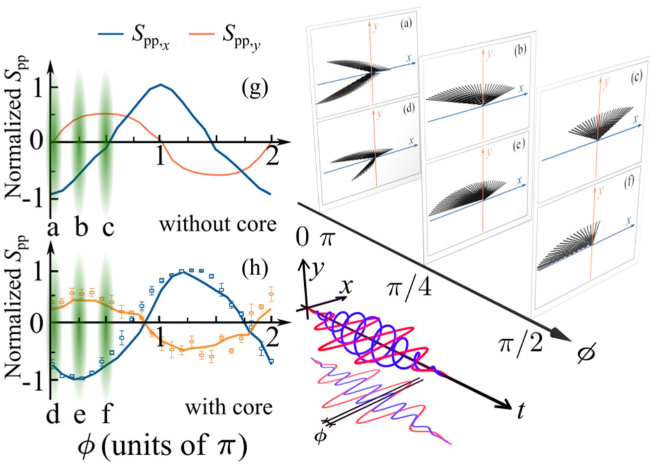

FIG. 9. The THz yields $S_{\mathrm{pp},\sigma}(\varepsilon = 0, \phi)$ and the distributions of a photoelectron wave packet as a function of time delay ϕ in two-color laser fields of $\varepsilon = 0$ as shown in the bottom-right inset, with the same notation as in Fig. 8.

relatively high asymmetry towards the $-x$ direction, as shown by $S_{\mathrm{pp},x}$ in region "a" of panel (g). The two branches have y components of opposite signs but roughly the same amplitude, resulting in vanishing asymmetry and $S_{\mathrm{pp},y} \simeq 0$. In the presence of the Coulomb potential, the high-weight trajectories in the lower branch undergo "hard" rescattering with the parent ion, leading to the recapture by the parent ion to form Rydberg states [33]. While the recaptured electron contributes to HHGs, it reduces the number of effective trajectories. This reduction, as shown by the shrinking of the lower branch in panel (d), results in the increased asymmetry towards the positive y direction in region "d" of panel (h). When $\phi = \pi/4$, the wave packet without Coulomb interaction shows a relatively symmetric distribution about the y-axis, summing to a relatively small value of $S_{\mathrm{pp},x}$ in region "b" of panel (g), while the presence of the Coulomb potential maximizes the asymmetry, leading to the most efficient THz emission in the $-x$ direction, as shown in region "e" of panel (h). When $\phi = \pi/2$, the fanlike wave packet is shifted towards the $-x$ direction by the Coulomb potential. It increases the asymmetry on the x direction, while the asymmetry along the y direction is suppressed, as we compare $S_{\mathrm{pp},\sigma}$ in region "c" of panel (g) and "f" of panel (h). The pattern analysis of the wave packet indicates that the distribution of the photoelectron wave packet, particularly the symmetry during its propagation, is inherently embedded in TWGs. In addition, we examined the PP curves of THz with the Coulomb potential in two directions as shown in Figs. 8(h) and 9(h), corresponding to $\varepsilon = 1$ and 0 in Figs. 2(f) and 2(g) in the main text. By analyzing the cases for $\phi = 0$ (in regions "c" and "e") and $\phi = \pi/2$ (in regions "d" and "f"), comparing the results of THz polarization as illustrated in Figs. 3(e)–3(h) in the main text, we observed the THz yield in the x and y directions, corresponding to the projection of THz polarization in the x and y planes. Therefore, examining the influence of the Coulomb potential on THz yield in two directions is essentially equivalent to analyzing its effects on THz polarization.

APPENDIX D: COULOMB EFFECTS ON THZ WAVE EMISSION

The TWG is calculated using the classical trajectory Monte Carlo (CTMC) method, which has been widely applied to understand strong field physics from a classical perspective. When subject to an intense light field $E(t)$, an atom can be ionized via tunneling ionization, by which the electron tunnels through the atomic potential barrier in the plane of the laser polarization. The ionization rate, as described by the Ammosov, Delone, and Krainov tunneling theory [34,35], is given by $w_i = w(t_0^{(i)})w(p_\perp^{(i)})$, dependent on both the tunneling time $t_0^{(i)}$ and the initial transverse momentum $p_\perp^{(i)}$ (perpendicular to the instantaneous laser polarization). Here, index i is used to label the ith photoelectron. The $t_0^{(i)}$-dependent weight is given by

$$w\left(t_0^{(i)}\right) = 4\left[\frac{2\kappa^2}{\left|E\left(t_0^{(i)}\right)\right|}\right]^{\frac{2}{\kappa}-1} \exp\left[-\frac{2\kappa^3}{3\left|E\left(t_0^{(i)}\right)\right|}\right],$$

with $\kappa = \sqrt{2I_\mathrm{p}}$ and I_p the atomic ionization potential, and the $p_\perp^{(i)}$-dependent weight reads

$$w(p_\perp^{(i)}) = \frac{\kappa}{|E(t_0)|}\left(\frac{p_\perp^{(i)}}{\pi}\right) \exp\left[\frac{-\kappa(p_\perp^{(i)})^2}{\left|E\left(t_0^{(i)}\right)\right|}\right].$$

When sampling for the simulation, both $t_0^{(i)}$ and $p_\perp^{(i)}$ are independent random variables of uniform distribution, $t_0^{(i)} \sim \mathcal{U}(0, T_0)$ and $p_\perp^{(i)} \sim \mathcal{U}(-3\sigma_\perp, 3\sigma_\perp)$, with $\sigma_\perp = \sqrt{E(t_0)/\kappa}$ and T_0 the pulse duration.

When subject to both the external light and Coulomb fields, the photoelectron propagates following the equation of motion

$$\frac{d^2}{dt^2}\boldsymbol{r}(t) = -\boldsymbol{E}(t) - \frac{\boldsymbol{r}(t)}{|\boldsymbol{r}(t)|^3}$$

with $\boldsymbol{r}(t)$ its trajectory. For the ith trajectory, at the initial time $t_0^{(i)}$, the initial longitudinal momentum is 0 ($p_\parallel^{(i)} = 0$) and the initial transverse momentum is given by $\boldsymbol{p}_0^{(i)} \equiv [p_{0x}^{(i)}, p_{0y}^{(i)}, p_{0z}^{(i)}] = p_\perp^{(i)}[-\cos\alpha\sin\beta, \sin\alpha\sin\beta, \cos\beta]$, where α is the angle between the instantaneous electric field $\boldsymbol{E}(t_0^{(i)})$ and the positive x-axis, and β is the angle between $p_\perp^{(i)}$ and the positive z direction [24,36]. The initial position is given by $\boldsymbol{r}_0^{(i)} \equiv [r_{0x}^{(i)}, r_{0y}^{(i)}, r_{0z}^{(i)}] = r_0^{(i)}[\cos\alpha, \sin\alpha, 0]$ in terms of the classical turning point $r_0^{(i)} = -I_\mathrm{p}/|E(t_0^{(i)})|$ [37,38].

All trajectories contribute to the ensemble, $\langle\boldsymbol{r}(t)\rangle = \sum_i w_i\Theta(t - t_0^{(i)})\boldsymbol{r}_i(t)$, and the acceleration of the ensemble reads $\langle\boldsymbol{a}(t)\rangle = \sum_i w_i\Theta(t - t_0^{(i)})\boldsymbol{a}_i(t)$. The measurable THz signal is retrieved as the low-frequency radiation produced by the motion of the ensemble. We apply the Fourier transform to $\boldsymbol{a}(t)$, $\mathscr{F}\{\langle\boldsymbol{a}(t)\rangle\}(\omega)$, and we filter out the low-frequency component when $\omega \to 0$ to extract the THz wave. Finally, the dependence distributions $S_{\mathrm{pp},\sigma}(\varepsilon, \phi)$ ($\sigma = x, y$) are evaluated as shown by Figs. 2(f) and 2(g) in the main text.

1. Contribution of the laser field on the THz wave

The radiation derives from the acceleration of the ensemble $\boldsymbol{a}(t) = \sum_i w_i\Theta(t - t_0^{(i)})\boldsymbol{a}_i(t)$. Defining $\tilde{\boldsymbol{a}}(\omega) \equiv \mathscr{F}\{\boldsymbol{a}(t)\}(\omega)$

its frequency-domain counterpart, the contribution to the radiation consists of two parts, $\tilde{\boldsymbol{a}}_0(\omega)$ solely from the laser field and $\tilde{\boldsymbol{a}}_C(\omega)$ from the Coulomb interaction,

$$\tilde{\boldsymbol{a}}(\omega) = \tilde{\boldsymbol{a}}_0(\omega) + \tilde{\boldsymbol{a}}_C(\omega). \tag{D1}$$

Given the analytic expression of $\boldsymbol{E}(t)$, the acceleration for the radiation reads

$$\tilde{\boldsymbol{a}}_0(\omega) = -\sum_i w_i \int_{t_0^{(i)}}^{\infty} dt e^{-i\omega t}\boldsymbol{E}(t). \tag{D2}$$

As discussed in Appendix D, the initial transverse momentum presents a normal distribution centering at $p_\perp = 0$. Thus, we only consider the contribution of trajectories of the largest weight $\boldsymbol{v}_i(t_0^{(i)}) = 0$. We assume that the two-color $(\omega - 2\omega)$ laser fields $\boldsymbol{E}(t) = [E_x(t), E_y(t), 0]$ have equal electric amplitudes, and the ω-field is circularly polarized as described by

$$E_x(t) = Ef(t)\left[\frac{1}{\sqrt{1+\varepsilon_1^2}}\cos(\omega_1 t + \phi_0) + \frac{k}{\sqrt{2}}\cos(2\omega_1 t + \phi_0 + \phi)\right], \tag{D3}$$

$$E_y(t) = Ef(t)\left[\frac{\varepsilon_1}{\sqrt{1+\varepsilon_1^2}}\sin(\omega_1 t + \phi_0) + \frac{k}{\sqrt{2}}\sin(2\omega_1 t + \phi_0 + \phi)\right] \tag{D4}$$

with $\phi \in [0, 2\pi]$ the phase delay between ω and 2ω laser pulses, and $\phi_0 = \pi/2$ is the initial phase of the laser fields. The $k = \frac{1}{\sqrt{2}}$ is the field-strength ratio of ω and 2ω laser pulses. The envelope $f(t) = e^{-\frac{(t-t_c)^2}{2\sigma^2}}$ is given by a Gaussian profile. The amplitude of the electric fields $E = 0.07$ a.u. is used for both CTMC and PC calculations. The ellipticity of the ω-field is tunable, $\varepsilon_1 \in [-1, 1]$. As ϕ_0 is a constant and does not affect the subsequent calculations, we omit it in the following computations and add it in the last step. To evaluate $\int_{t_0^{(i)}}^{\infty} dt\boldsymbol{E}(t)e^{-i\omega t}$ in Eq. (D2), we first solve the half-sided Fourier transform of trigonometric functions as presented in Eqs. (D3) and (D4),

$$\begin{aligned}
&\int_{t_0}^{\infty} dt e^{-\frac{(t-t_c)^2}{2\sigma^2}}\sin(\omega_1 t + \phi)e^{-i\omega t} \\
&= i\sqrt{\frac{\pi}{8}}\sigma\left[\sum_{\pm}(\pm)e^{-i\phi_\pm(t_0) - \frac{(\omega_\pm\sigma)^2}{2}} + e^{-\frac{(t_0-t_c)^2}{2\sigma^2}}\sum_{\pm}(\mp)e^{-i\phi_\pm(t_0)}w\left(i\frac{t_0-t_c}{\sqrt{2}\sigma} - \frac{\omega_\pm\sigma}{\sqrt{2}}\right)\right] \\
&\times \int_{t_0}^{\infty} dt e^{-\frac{(t-t_c)^2}{2\sigma^2}}\cos(\omega_1 t + \phi)e^{-i\omega t} \\
&= \sqrt{\frac{\pi}{8}}\sigma\left[\sum_{\pm} e^{-i\phi_\pm(t_0) - \frac{(\omega_\pm\sigma)^2}{2}} - e^{-\frac{(t_0-t_c)^2}{2\sigma^2}}\sum_{\pm} e^{-i\phi_\pm(t_0)}w\left(i\frac{t_0-t_c}{\sqrt{2}\sigma} - \frac{\omega_\pm\sigma}{\sqrt{2}}\right)\right],
\end{aligned}$$

where $\omega_\pm = \omega \pm \omega_1$, $\phi_\pm(t_0) = \omega_\pm t_0 \pm \phi$, and $w(z)$ is the Faddeeva function.

In the low-frequency domain where $\omega \ll \omega_1$, the first term in both integrals vanishes as $e^{-\frac{(\omega_\pm\sigma)^2}{2}} \simeq 0$, and the above integrals can be approximated by

$$\begin{aligned}
&\int dt e^{-\frac{(t-t_c)^2}{2\sigma^2}}\sin(\omega_1 t + \phi)e^{-i\omega t} \\
&\simeq i\sqrt{\frac{\pi}{8}}\sigma e^{-\frac{(t_0-t_c)^2}{2\sigma^2}}\sum_{\pm}(\mp)e^{-i\phi_\pm(t_0)}w\left(i\frac{t_0-t_c}{\sqrt{2}\sigma} - \frac{\omega_\pm\sigma}{\sqrt{2}}\right), \\
&\int dt e^{-\frac{(t-t_c)^2}{2\sigma^2}}\cos(\omega_1 t + \phi)e^{-i\omega t} \\
&\simeq -\sqrt{\frac{\pi}{8}}\sigma e^{-\frac{(t_0-t_c)^2}{2\sigma^2}}\sum_{\pm} e^{-i\phi_\pm(t_0)}w\left(i\frac{t_0-t_c}{\sqrt{2}\sigma} - \frac{\omega_\pm\sigma}{\sqrt{2}}\right).
\end{aligned}$$

For the two-color laser fields of Eqs. (D3) and (D4),

$$\begin{aligned}
&\int_{t_0^{(i)}}^{\infty} dt E_x(t)e^{-i\omega t} \\
&= \frac{E_1}{\sqrt{1+\varepsilon_1^2}}\int_{t_0^{(i)}}^{\infty} dt f_1(t)\cos(\omega_1 t)e^{-i\omega t} + \frac{E_1}{\sqrt{2}}\int_{t_0^{(i)}}^{\infty} dt f_1(t)\cos(2\omega_1 t + \phi)e^{-i\omega t} \\
&= -E_1\sqrt{\frac{\pi}{8}}\sigma e^{-\frac{(t_0-t_c)^2}{2\sigma^2}}\left[\frac{\sum_\pm e^{-i\phi_\pm(t_0)}w\left(i\frac{t_0-t_c}{\sqrt{2}\sigma} - \frac{\omega_\pm\sigma}{\sqrt{2}}\right)}{\sqrt{1+\varepsilon_1^2}} + k\frac{\sum_\pm e^{-i\phi_{2\pm}(t_0)}w\left(i\frac{t_0-t_c}{\sqrt{2}\sigma} - \frac{\omega_{2\pm}\sigma}{\sqrt{2}}\right)}{\sqrt{2}}\right],
\end{aligned} \tag{D5}$$

$$\begin{aligned}
&\int_{t_0^{(i)}}^{\infty} dt E_y(t)e^{-i\omega t} \\
&= \frac{E_1\varepsilon_1}{\sqrt{1+\varepsilon_1^2}}\int_{t_0^{(i)}}^{\infty} dt f_1(t)\sin(\omega_1 t)e^{-i\omega t} + \frac{E_1}{\sqrt{2}}\int_{t_0^{(i)}}^{\infty} dt f_1(t)\sin(2\omega_1 t + \phi)e^{-i\omega t} \\
&= iE_1\sqrt{\frac{\pi}{8}}\sigma e^{-\frac{(t_0-t_c)^2}{2\sigma^2}}\left[\frac{\varepsilon_1\sum_\pm(\mp)e^{-i\phi_\pm(t_0)}w\left(i\frac{t_0-t_c}{\sqrt{2}\sigma} - \frac{\omega_\pm\sigma}{\sqrt{2}}\right)}{\sqrt{1+\varepsilon_1^2}} + k\frac{\sum_\pm(\mp)e^{-i\phi_{2\pm}(t_0)}w\left(i\frac{t_0-t_c}{\sqrt{2}\sigma} - \frac{\omega_{2\pm}\sigma}{\sqrt{2}}\right)}{\sqrt{2}}\right],
\end{aligned} \tag{D6}$$

where $\omega_{2\pm} = \omega \pm 2\omega_1$ and $\phi_{2\pm}(t) = 2\omega_\pm t_0 \pm \phi$. With Eqs. (D5) and (D6), we evaluate the THz yield contributed by the trajectory launched at different times, and then we obtain the distribution of $S_{\mathrm{pp},\sigma}(\varepsilon, \phi)$ from C-C fields to C-L fields as shown in Figs. 10(a) and 10(b), in good agreement with distributions evaluated by the PC model [Figs. 2(b) and 2(c) in the main text].

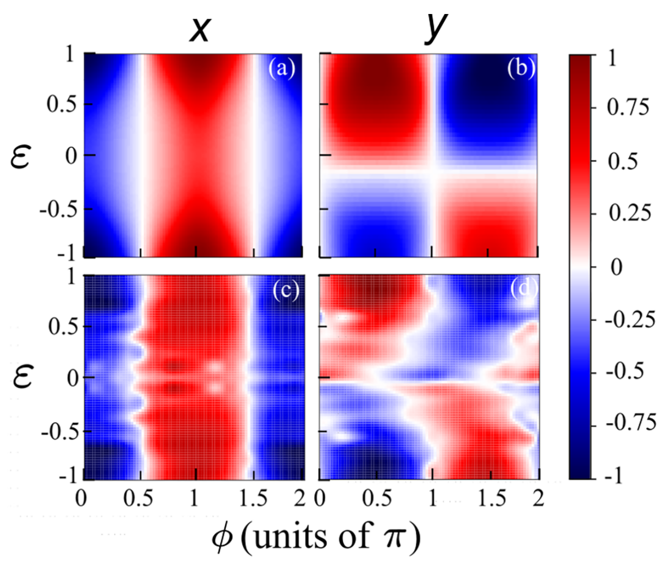

FIG. 10. The PP distribution in the x-direction, $S_{\mathrm{pp},x}(\varepsilon,\phi)$, is shown for a CTMC analytic calculation (a) without Coulomb potential and (c) with Coulomb potential. Similarly, the corresponding distributions of PP in the y-direction, $S_{\mathrm{pp},y}(\varepsilon,\phi)$, are shown in the right panels (b) and (d).

2. Derivation of time-averaged photoelectron trajectories

When the released photoelectron is rapidly pulled away by the external light field and never returns close to the ionic core, the second term $\tilde{\boldsymbol{a}}_C(t)$ induced by the Coulomb potential usually can be described by the first-order perturbation, $\tilde{\boldsymbol{a}}_C^{(0)}(t) = -\frac{\boldsymbol{r}_0(t)}{|\boldsymbol{r}_0(t)|^3}$ with regard to the zeroth-order trajectory $\boldsymbol{r}_0(t)$ without Coulomb correction,

$$\boldsymbol{r}_0(t) = \int_{t_0}^{t} dt' \int_{t_0}^{t'} dt'' \boldsymbol{a}_0(t'') + \boldsymbol{v}_0(t-t_0) + \boldsymbol{r}_0. \quad \text{(D7)}$$

With $\boldsymbol{a}_0(t) = -\boldsymbol{E}(t)$, substituting Eq. (D3) into Eq. (D7), the component in the x direction reads

$$r_x(t) = -\frac{E}{\sqrt{1+\varepsilon_1^2}} \int_{t_0}^{t} dt' \int_{t_0}^{t'} dt'' f(t'')\cos(\omega_1 t'') - \frac{kE}{\sqrt{2}} \int_{t_0}^{t} dt' \int_{t_0}^{t'} dt'' f(t'')\cos(2\omega_1 t'' + \phi) + v_{x0}(t-t_0) + r_{x0}.$$

The relatively long pulse used in TWG usually enables us to solve the integral considering the slowly varying envelope,

$$\int_{t_0}^{t} dt' \int_{t_0}^{t'} dt'' f_1(t'')\cos(\omega_1 t'') \simeq -\frac{f_1(t)\cos(\omega_1 t)}{\omega_1^2} + \frac{f_1(t_0)\cos(\omega_1 t_0)}{\omega_1^2} - \frac{f_1(t_0)\sin(\omega_1 t_0)}{\omega_1}(t-t_0)$$

and we obtain

$$r_x(t) = -\frac{E_1}{\sqrt{1+\varepsilon_1^2}} \frac{f_1(t_0)}{\omega_1^2}[-\cos(\omega_1 t) + \cos(\omega_1 t_0) - \omega_1 \sin(\omega_1 t_0)(t-t_0)] - \frac{kE_1}{\sqrt{2}} \frac{f_1(t_0)}{4\omega_1^2}[-\cos(2\omega_1 t + \phi) + \cos(2\omega_1 t_0 + \phi) - 2\omega_1 \sin(2\omega_1 t_0 + \phi)(t-t_0)] + v_{x0}(t-t_0) + r_{x0}.$$

In each set of square brackets, the first term describes the oscillation of optical frequency; the second term, being constant, derives from the initial condition of the trajectory; the third term, being linear to the propagation time, describes the overall profile of the trajectory on the long timescale.

To describe the TWG, the $r_x(t)$ can be simplified with the low-pass filter by neglecting the first term of short-time oscillation,

$$r_x(t) \simeq \frac{E_1 f_1(t_0)}{\omega_1}\left[\frac{\sin(\omega_1 t_0)}{\sqrt{1+\varepsilon_1^2}} + k\frac{\sin(2\omega_1 t_0 + \phi)}{2\sqrt{2}}\right](t-t_0) - \frac{E_1 f_1(t_0)}{\omega_1^2}\left[\frac{\cos(\omega_1 t_0)}{\sqrt{1+\varepsilon_1^2}} + k\frac{\cos(2\omega_1 t_0 + \phi)}{4\sqrt{2}}\right] + v_{x0}(t-t_0) + r_{x0}.$$

Similarly, we have the component in the y direction,

$$r_y(t) \simeq \frac{-E_1 f_1(t_0)}{\omega_1}\left[\frac{\varepsilon_1\cos(\omega_1 t_0)}{\sqrt{1+\varepsilon_1^2}} + k\frac{\cos(2\omega_1 t_0 + \phi)}{2\sqrt{2}}\right] \times (t-t_0) - \frac{E_1 f_1(t_0)}{\omega_1^2}\left[\frac{\varepsilon_1\sin(\omega_1 t_0)}{\sqrt{1+\varepsilon_1^2}} + k\frac{\sin(2\omega_1 t_0 + \phi)}{4\sqrt{2}}\right] + v_{y0}(t-t_0) + r_{y0}.$$

Both expressions take the slope-intercept form,

$$r_x(t) = a_x(t-t_0) + b_x, \quad \text{(D8)}$$

$$r_y(t) = a_y(t-t_0) + b_y, \quad \text{(D9)}$$

where

$$a_x = \frac{E_1 f_1(t_0)}{\omega_1}\left[\frac{\sin(\omega_1 t_0)}{\sqrt{1+\varepsilon_1^2}} + k\frac{\sin(2\omega_1 t_0 + \phi)}{2\sqrt{2}}\right],$$

$$b_x = -\frac{E_1 f_1(t_0)}{\omega_1^2}\left[\frac{\cos(\omega_1 t_0)}{\sqrt{1+\varepsilon_1^2}} + k\frac{\cos(2\omega_1 t_0 + \phi)}{4\sqrt{2}}\right] + v_{x0}(t-t_0) + r_{x0},$$

$$a_y = -\frac{E_1 f_1(t_0)}{\omega_1}\left[\frac{\varepsilon_1\cos(\omega_1 t_0)}{\sqrt{1+\varepsilon_1^2}} + k\frac{\cos(2\omega_1 t_0 + \phi)}{2\sqrt{2}}\right],$$

$$b_y = -\frac{E_1 f_1(t_0)}{\omega_1^2}\left[\frac{\varepsilon_1\sin(\omega_1 t_0)}{\sqrt{1+\varepsilon_1^2}} + k\frac{\sin(2\omega_1 t_0 + \phi)}{4\sqrt{2}}\right] + v_{y0}(t-t_0) + r_{y0}.$$

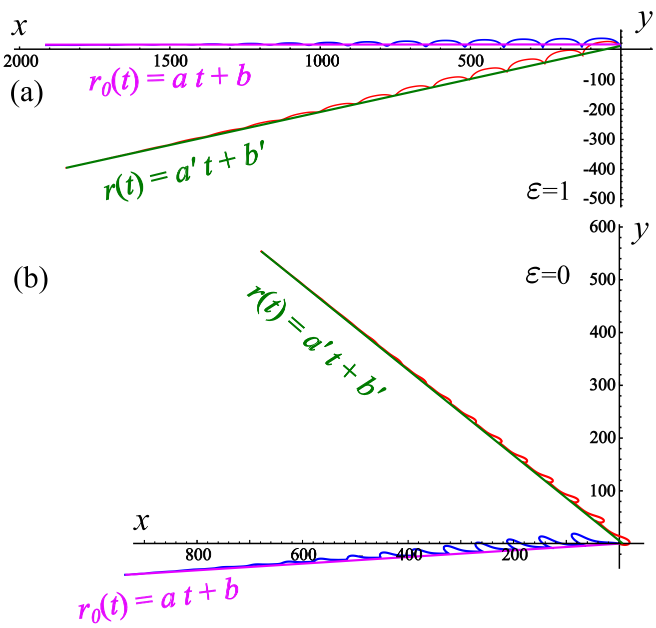

FIG. 11. The typical photoelectron trajectories are shown in (a) and (b) when $\varepsilon_1 = 1$ and $\varepsilon_1 = 0, \phi = 0$, respectively. Trajectory $\boldsymbol{r}_0(t)$ without Coulomb potential (blue) and its approximation evaluated by Eqs. (D8) and (D9) with a low-pass filter (purple). The corresponding Coulomb-corrected trajectory $\boldsymbol{r}(t)$ (red) and its approximation evaluated by Eqs. (D8) and (D9) but with characteristic parameters a'_σ and b'_σ substituted by the ones for $\boldsymbol{r}(t)$ (green).

Typical trajectories $\boldsymbol{r}_0(t)$ and their approximation with a low-pass filter are illustrated in Fig. 11. When $\varepsilon = 1$, the long-term trajectory $\boldsymbol{r}_0(t)$ evaluated by Eqs. (D8) and (D9) roughly agrees with the numerical solution $\boldsymbol{r}(t)$, since the Coulomb potential only perturbatively affects the motion of the photoelectron. When $\varepsilon = 0$, the close approach of the electron back to the parent ion during its propagation incurs strong a Coulomb interaction that dramatically alters the photoelectron trajectory, thereby invalidating the use of $\boldsymbol{r}_0$ for the calculation. Nevertheless, trajectory $\boldsymbol{r}(t)$ in the long term still presents a straight-line path as depicted by Eqs. (D8) and (D9), but with characteristic parameters a'_σ and b'_σ substituted by the ones for Coulomb-corrected trajectories. Therefore, it is straightforward to derive the contribution of the Coulomb interaction to the radiation, $\boldsymbol{a}_C(t) = -\frac{\boldsymbol{r}(t)}{|\boldsymbol{r}(t)|^3}$, with $\boldsymbol{r}(t)$ approximated by a straight line of characteristic parameters.

3. Contribution of the Coulomb potential on the THz wave

Denoting the Coulomb correction $\boldsymbol{a}_C(t)$ in the frequency domain as $\tilde{\boldsymbol{a}}_C(\omega)$, we have

$$\tilde{\boldsymbol{a}}_C(\omega) = -\int_{-\infty}^{\infty} dt\,\Theta(t - t_0)\frac{\boldsymbol{r}(t)}{|\boldsymbol{r}(t)|^3}e^{-i\omega t}. \tag{D10}$$

Substituting $\boldsymbol{r}(t)$ by the approximated components Eqs. (D8) and (D9), the integrand $\frac{\boldsymbol{r}(t)}{|\boldsymbol{r}(t)|^3}$ can be expressed explicitly as a function of t,

$$\frac{r_\sigma}{|\boldsymbol{r}|^3} = \frac{a_\sigma t + c_\sigma}{|\boldsymbol{a}|^3(t^2 + c)^{3/2}}, \tag{D11}$$

where $\boldsymbol{a} = (a_x, a_y)$, $\boldsymbol{b} = (b_x, b_y)$, $c_\sigma = b_\sigma - a_\sigma\frac{\boldsymbol{a}\cdot\boldsymbol{b}}{\boldsymbol{a}^2}$, $c = \frac{\boldsymbol{a}^2\boldsymbol{b}^2 - (\boldsymbol{a}\cdot\boldsymbol{b})^2}{\boldsymbol{a}^2}$, and we have applied the substitution $t \to t - t_0 + \frac{\boldsymbol{a}\cdot\boldsymbol{b}}{\boldsymbol{a}^2}$. Thus the component of Eqs. (D10) reads

$$\tilde{a}_{C,\sigma}(\omega) = -\frac{1}{|\boldsymbol{a}|^3}e^{-i\omega\left(t_0 - \frac{\boldsymbol{a}\cdot\boldsymbol{b}}{\boldsymbol{a}^2}\right)}\int_{\frac{\boldsymbol{a}\cdot\boldsymbol{b}}{\boldsymbol{a}^2}}^{\infty} dt\,\frac{a_\sigma t + c_\sigma}{(t^2 + c)^{3/2}}e^{-i\omega t}. \tag{D12}$$

With a two-order convergence integrand, the integral will fast converge beyond a moderate T_c. This leads to the new truncated form

$$\tilde{a}_{C,\sigma}(\omega) = -\frac{1}{|\boldsymbol{a}|^3}e^{-i\omega\left(t_0 - \frac{\boldsymbol{a}\cdot\boldsymbol{b}}{\boldsymbol{a}^2}\right)}\int_{\frac{\boldsymbol{a}\cdot\boldsymbol{b}}{\boldsymbol{a}^2}}^{T_c} dt\,\frac{a_\sigma t + c_\sigma}{(t^2 + c)^{3/2}}e^{-i\omega t}. \tag{D13}$$

In the low-frequency limit $\omega \to 0$, $e^{-i\omega t} = \sum_n \frac{(-i)^n}{n!}\omega^n t^n$, we have

$$\tilde{a}_{C,\sigma}(\omega) = -\frac{1}{|\boldsymbol{a}|^3}e^{-i\omega\left(t_0 - \frac{\boldsymbol{a}\cdot\boldsymbol{b}}{\boldsymbol{a}^2}\right)}\sum_n \frac{(-i)^n}{n!}\omega^n \times \int_{\frac{\boldsymbol{a}\cdot\boldsymbol{b}}{\boldsymbol{a}^2}}^{T_c} dt\,\frac{a_\sigma t^{n+1} + c_\sigma t^n}{(t^2 + c)^{3/2}} \tag{D14}$$

with the integral taking the analytical form in terms of the hypergeometric function $F(a, b; c; z)$,

$$\int dt\,\frac{a_\sigma t^{n+1} + c_\sigma t^n}{(t^2 + c)^{3/2}} = \frac{t^{n+1}}{c^{3/2}}\left[\frac{a_\sigma t}{n+2}F\left(\frac{3}{2}, 1 + \frac{n}{2}; 2 + \frac{n}{2}; -\frac{t^2}{c}\right) + \frac{c_\sigma}{n+1}F\left(\frac{3}{2}, \frac{1+n}{2}; \frac{3+n}{2}; -\frac{t^2}{c}\right)\right].$$

The first two-order terms of $\tilde{a}_{C,\sigma}(\omega)$ are given by

$$\begin{aligned}
\tilde{a}^{(1)}_{C,\sigma} &= -\frac{1}{|\boldsymbol{a}|^3}e^{-i\omega\left(t_0 - \frac{\boldsymbol{a}\cdot\boldsymbol{b}}{\boldsymbol{a}^2}\right)}\left\{\frac{a_\sigma c\left(\sqrt{\frac{t^2+c}{c}} - 1\right) + c_\sigma t}{c\sqrt{t^2 + c}} + \left[a_\sigma - a_\sigma \operatorname{arcsinh}\left(\frac{t}{\sqrt{c}}\right) - \frac{3c_\sigma}{\sqrt{c}}\right]i\omega\right\}\Bigg|_{\frac{\boldsymbol{a}\cdot\boldsymbol{b}}{\boldsymbol{a}^2}}^{T_c} \\
&= -\frac{1}{|\boldsymbol{a}|^3}e^{-i\omega\left(t_0 - \frac{\boldsymbol{a}\cdot\boldsymbol{b}}{\boldsymbol{a}^2}\right)}\left\{\left(\frac{a_\sigma}{\sqrt{c}} + \frac{c_\sigma}{c}\right) + \left[a_\sigma - a_\sigma \operatorname{arcsinh}\left(\frac{T_c}{\sqrt{c}}\right) - \frac{3c_\sigma}{\sqrt{c}}\right]i\omega\right\} \\
&\approx -\frac{1}{|\boldsymbol{a}|^3}e^{-i\omega\left(t_0 - \frac{\boldsymbol{a}\cdot\boldsymbol{b}}{\boldsymbol{a}^2}\right)}\left(\frac{a_\sigma}{\sqrt{c}} + \frac{c_\sigma}{c}\right).
\end{aligned} \tag{D15}$$

As higher-order terms are negligibly small compared to $\tilde{a}_{C,\sigma}(\omega)$, here we only consider the zeroth term. This zeroth-order justification is consistent with the slowly varying properties of $e^{-i\omega t}$ at low ω, which is of almost constant duration in the fast convergence of the original function in $[\frac{\boldsymbol{a}\cdot\boldsymbol{b}}{\boldsymbol{a}^2}, T_c]$. Once given the characteristic parameters a_σ, b_σ of photoelectron motions, the Coulomb contribution to the radiation can be evaluated by Eq. (D15).

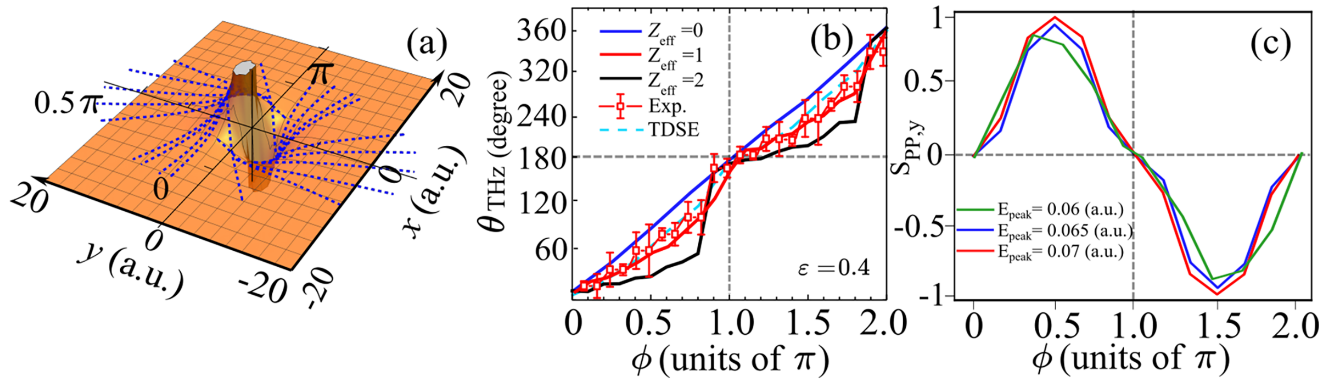

FIG. 12. Scheme of sketching the local potential by classical trajectories. (a) "Wire sculpture" of the local potential. The surface represents the x-component of $-\nabla V(\boldsymbol{r})$, and each trajectory (dashed line) represents the component of $\boldsymbol{a}_C(\boldsymbol{r}) \equiv \boldsymbol{a}_C(\boldsymbol{r}(t)) = \boldsymbol{a}_C(t)$ that can be acquired from all-optical measurement. By scanning over the time delay ϕ, the set of classical trajectories $\{\boldsymbol{a}_C(\boldsymbol{r})\}$ sketches the potential energy surface. (b) The dependence of the THz polarization direction $\theta_{\rm THz}(\phi)$ on time delay ϕ with different effective charge $Z_{\rm eff}$. (c) The normalized components of y-polarized peak-to-peak values of THz electric fields, $S_{{\rm pp},y}(\phi)$, predicted by TDSE simulation at $\varepsilon = 0.4$ with different intensities of laser fields $E_{\rm peak}$.

In Fig. 10, we present a comparison of the distribution of PP values obtained by analytical calculation with Eqs. (D5), (D6), and (D15). The distribution of the y component shows a clear phase shift, as measured in experiment, justifying the analysis of the trajectory-based model.

APPENDIX E: DETAILS OF THE RECONSTRUCTION PROCEDURE

The all-optical reconstruction is conceptually straightforward concerning the classical motion of the photoelectron. The laser fields can be manipulated by scanning the time delay ϕ to control photoelectron trajectories to traverse the region of interest around the parent core. Taking the two-color fields of circular and elliptical polarizations, for instance, the tunneling ionization with varying ϕ results in the emission of photoelectrons in different directions.

If a sufficiently broad spectrum of the radiated field, $\tilde{\boldsymbol{E}}_{\rm rad}(\omega)$, can be acquired, the reconstructed acceleration of a photoelectron, $\boldsymbol{a}(t) = \boldsymbol{E}_{\rm rad}(t)$, in principle, enables us to trace the local potential, $\nabla V(\boldsymbol{r}) = -\boldsymbol{a}_C(\boldsymbol{r}(t)) = -[\boldsymbol{a}(t) + \boldsymbol{a}_{\boldsymbol{0}}(t)]$. The theoretical testing indicates that the reconstruction method requires a wide bandwidth measurement exceeding 280 THz in order to accurately sketch the Coulomb potential. From a classical perspective, as in Fig. 7(a), trajectories of different ϕ contain information about the effective potential in different regions. Multiple trajectories under different ϕ, therefore, sketch the contour of $\nabla V(\boldsymbol{r})$ as analogous to the mesh representation of an object in an artistic wire sculpture (see Fig. 12).

The reconstruction procedure is implemented using the following steps: (i) For each ϕ, measure $\tilde{\boldsymbol{E}}_{\rm rad}(\omega)$ including Coulomb effects, as well as the intensities of two-color fields, which are used to calculate $\tilde{\boldsymbol{a}}_0(\omega)$ without Coulomb effects by means of either PC or CTMC without Coulomb correction. (ii) Filter out the rapidly varying oscillation of $\tilde{\boldsymbol{E}}_{\rm rad}(\omega)$ and $\tilde{\boldsymbol{a}}_0(\omega)$ using a low-pass filter $\mathscr{W}$ while retaining the slowly varying component $\mathscr{W}[\tilde{\boldsymbol{E}}_{\rm rad}(\omega)]$ and $\mathscr{W}[\tilde{\boldsymbol{a}}_0(\omega)]$. (iii) Obtain $\boldsymbol{a}(t) = \mathscr{F}^{-1}\{\mathscr{W}[\tilde{\boldsymbol{E}}_{\rm rad}(\omega)]\}$ and $\boldsymbol{a}_0(t) = \mathscr{F}^{-1}\{\mathscr{W}[\tilde{\boldsymbol{a}}_0(\omega)]\}$ by performing Fourier transform, which gives the accelerations induced by the guiding-center trajectories [29]. (iv) Obtain the acceleration induced by the Coulomb potential with $\boldsymbol{a}_C(t) = \boldsymbol{a}(t) - \boldsymbol{a}_0(t)$. Employing $\boldsymbol{a}_C(t)$ and $\boldsymbol{r}(t) = \iint \boldsymbol{a}_C(t)\,{\rm d}t$, $\nabla V(\boldsymbol{r})$ can be reconstructed and depicted as blue dashed lines in Fig. 5(a) in the main text. (v) Traverse ϕ to sketch the shape of the local potential. We can find that the experimental curve matches the simulation one at $Z_{\rm eff} = 1$ very well in Fig. 5(b) in the main text, which validates the effective charge $Z_{\rm eff} = 1$ used in our model.

It should be noted that in the reconstruction procedure, ε can be neither too small nor too large. When $\varepsilon = 0$, the photoelectrons are mostly oscillating along the x-axis, which leads to the same θ for all phases. In this case, Z and ϕ_0 could not be determined. The photoelectron is also prone to recollide with the parent core, which is unfavorable to the TWG. When $\varepsilon = 1$, the Coulomb potential induces an equal rotation of the emission direction for all ϕ, resulting in a similar $\theta(\phi)$ profile while only differing by a shift along ϕ. Since $\phi = 0$ is technically difficult to determine precisely, $\varepsilon = 1$ is not recommended for the parameter retrieval. Here, as shown by Fig. 4(a) in the main text, $\varepsilon = 0.4$ is chosen to optimize the outcome for the method.

As mentioned in the main text, even though experimental results provide spectra limited to 0.1–3 THz, information about the Coulomb potential (such as a key parameter of the effective potential $Z_{\rm eff}$) in the process of photoelectron ionization can still be obtained by measuring the polarization direction of THz radiation.

As shown in Fig. 2(c) of Ref. [30], in which the experimental result of the emitting angle and the two-color phase-of-phase (POP) under different laser intensities (energies) in krypton atoms was measured using attoclock techniques, with an increase in electric field energy, the influence of the Coulomb potential diminishes, which means that $Z_{\rm eff}$ decreases. Those authors illustrate three cuts of the POP spectrum (the POP slope with respect to the photoelectron emitting angle) along energies of 4, 8, and 16 eV, respectively [30]. According to the conclusion drawn in [26], the emission angle of photoelectrons aligns with the polarization direction of THz radiation. Consequently, the $\Phi_{\rm POP}$ and photoelectron emitting angle in Ref. [30] directly correspond to ϕ and $\theta_{\mathrm{THz}}(\phi)$ in our work. The curve depicting the relationship between emitting angle and POP transforms from a 45° linear slope to a double-step structure. This agrees with the trend obtained from our reconstruction algorithm in Fig. 8(b). It is noteworthy that in our approach, the phase delay ϕ of the two-color field can be determined in the experiment. As shown in Fig. 8(b), the direction of TWG polarization θ_{THz} ($\phi = 0^\circ, 180^\circ$) $= 0^\circ, 180^\circ$ remains unchanged regardless of Z_{eff}. Thus, the phase $\phi = 0$ or $\phi = \pi$ can be determined when $\theta_{\mathrm{THz}} = 0^\circ, 180^\circ$ in the experiment. Furthermore, to verify the proposed method, we conducted TDSE simulations to investigate the y-polarized THz yields $S_{\mathrm{PP},y}$ as a function of ϕ and the strengths of ω electric fields E_{peak}. As illustrated in Fig. 8(c), the minima of $S_{\mathrm{PP},y}(\phi)$ consistently occur at $\phi = 0$ and $\phi = \pi$ for $E_{\mathrm{peak}} = 0.06, 0.065, 0.07$ (a.u.). The TDSE simulation not only corroborates the reconstruction methodology in panel (b), but it also indicates the capability to determine the absolute phase delay ϕ of the two-color fields.

[1] J. Itatani, J. Levesque, D. Zeidler, H. Niikura, H. Pépin, J. C. Kieffer, P. B. Corkum, and D. M. Villeneuve, Nature (London) **432**, 867 (2004).

[2] C. Vozzi, M. Negro, F. Calegari, G. Sansone, M. Nisoli, S. De Silvestri, and S. Stagira, Nat. Phys. **7**, 822 (2011).

[3] D. Shafir, H. Soifer, B. D. Bruner, M. Dagan, Y. Mairesse, S. Patchkovskii, M. Y. Ivanov, O. Smirnova, and N. Dudovich, Nature (London) **485**, 343 (2012).

[4] O. Pedatzur, G. Orenstein, V. Serbinenko, H. Soifer, B. D. Bruner, A. J. Uzan, D. S. Brambila, A. G. Harvey, L. Torlina, F. Morales, O. Smirnova, and N. Dudovich, Nat. Phys. **11**, 815 (2015).

[5] M. Lein, Phys. Rev. Lett. **94**, 053004 (2005).

[6] S. Baker, J. S. Robinson, C. A. Haworth, H. Teng, R. A. Smith, C. C. Chirilă, M. Lein, J. W. G. Tisch, and J. P. Marangos, Science **312**, 424 (2006).

[7] X.-B. Bian and A. D. Bandrauk, Phys. Rev. Lett. **113**, 193901 (2014).

[8] D. J. Cook and R. M. Hochstrasser, Opt. Lett. **25**, 1210 (2000).

[9] F. Brunel, J. Opt. Soc. Am. B **7**, 521 (1990).

[10] Y. Huang, C. Meng, X. Wang, Z. Lü, D. Zhang, W. Chen, J. Zhao, J. Yuan, and Z. Zhao, Phys. Rev. Lett. **115**, 123002 (2015).

[11] I. Babushkin, A. J. Galán, J. R. C. de Andrade, A. Husakou, F. Morales, M. Kretschmar, T. Nagy, V. Vaičaitis, L. Shi, D. Zuber, L. Bergé, S. Skupin, I. A. Nikolaeva, N. A. Panov, D. E. Shipilo, O. G. Kosareva, A. N. Pfeiffer, A. Demircan, M. J. J. Vrakking, U. Morgner, and M. Ivanov, Nat. Phys. **18**, 417 (2022).

[12] P. Eckle, M. Smolarski, P. Schlup, J. Biegert, A. Staudte, M. Schoeffler, H. G. Muller, R. Doerner, and U. Keller, Nat. Phys. **4**, 565 (2008).

[13] P. Eckle, A. N. Pfeiffer, C. Cirelli, A. Staudte, R. Doerner, H. G. Muller, M. Buettiker, and U. Keller, Science **322**, 1525 (2008).

[14] N. Camus, E. Yakaboylu, L. Fechner, M. Klaiber, M. Laux, Y. Mi, K. Z. Hatsagortsyan, T. Pfeifer, C. H. Keitel, and R. Moshammer, Phys. Rev. Lett. **119**, 023201 (2017).

[15] U. S. Sainadh, H. Xu, X. Wang, A. Atia-Tul-Noor, W. C. Wallace, N. Douguet, A. Bray, I. Ivanov, K. Bartschat, A. Kheifets, R. T. Sang, and I. V. Litvinyuk, Nature (London) **569**, E5 (2019).

[16] K. Y. Kim, J. H. Glownia, A. J. Taylor, and G. Rodriguez, Opt. Express **15**, 4577 (2007).

[17] Z. Zhou, D. Zhang, Z. Zhao, and J. Yuan, Phys. Rev. A **79**, 063413 (2009).

[18] K. Zhang, Y. Zhang, X. Wang, T.-M. Yan, and Y. H. Jiang, Photon. Res. **8**, 760 (2020).

[19] D. Azoury, O. Kneller, S. Rozen, B. D. Bruner, A. Clergerie, Y. Mairesse, B. Fabre, B. Pons, N. Dudovich, and M. Kruger, Nat. Photon. **13**, 54 (2019).

[20] W. Boutu, S. Haessler, H. Merdji, P. Breger, G. Waters, M. Stankiewicz, L. Frasinski, R. Taieb, J. Caillat, A. Maquet, P. Monchicourt, and B. Carre, Nat. Phys. **4**, 545 (2008).

[21] X. Zhou, R. Lock, W. Li, N. Wagner, M. M. Murnane, and H. C. Kapteyn, Phys. Rev. Lett. **100**, 073902 (2008).

[22] K. Y. Kim, A. J. Taylor, J. H. Glownia, and G. Rodriguez, Nat. Photon. **2**, 605 (2008).

[23] I. Babushkin, S. Skupin, A. Husakou, C. Köhler, E. Cabrera-Granado, L. Bergé, and J. Herrmann, New J. Phys. **13**, 123029 (2011).

[24] J. Liu, W. Chen, B. Zhang, J. Zhao, J. Wu, J. Yuan, and Z. Zhao, Phys. Rev. A **90**, 063420 (2014).

[25] D. Zhang, Z. Lü, C. Meng, X. Du, Z. Zhou, Z. Zhao, and J. Yuan, Phys. Rev. Lett. **109**, 243002 (2012).

[26] Y. Gao, Y. Zhang, K. Zhang, Z. Gan, T.-M. Yan, and Y. Jiang, Opt. Lett. **48**, 2575 (2023).

[27] Y. Zhang, K. Zhang, T.-M. Yan, and Y. Jiang, J. Phys. B **54**, 195401 (2021).

[28] X. Fan, Y. Gao, T.-M. Yan, Y. Jiang, and Y. Zhang, Opt. Express **31**, 86 (2023).

[29] J. Dubois, S. A. Berman, C. Chandre, and T. Uzer, Phys. Rev. Lett. **121**, 113202 (2018).

[30] M. Han, P. Ge, J. Wang, G. Zhenning, Y. Fang, X. Ma, Y. Yu, Y. Deng, H. J. Wörner, Q. Gong, and Y. Liu, Nat. Photon. **15**, 765 (2021).

[31] C. Meng, W. Chen, X. Wang, Z. Lü, Y. Huang, J. Liu, D. Zhang, Z. Zhao, and J. Yuan, Appl. Phys. Lett. **109**, 131105 (2016).

[32] K. Zhang, Y. Zhang, X. Wang, Z. Shen, T.-M. Yan, and Y. H. Jiang, Opt. Lett. **45**, 1838 (2020).

[33] J. Liu, J. Zhao, Y. Huang, X. Wang, and Z. Zhao, Phys. Rev. A **102**, 023109 (2020).

[34] M. V. Ammosov, N. B. Delone, and V. P. Krainov, Sov. Phys. JETP **64**, 1191 (1986).

[35] N. B. Delone and V. P. Krainov, J. Opt. Soc. Am. B **8**, 1207 (1991).

[36] J. Liu, Y. Fu, W. Chen, Z. Lü, J. Zhao, J. Yuan, and Z. Zhao, J. Phys. B **50**, 055602 (2017).

[37] L. D. Landau and L. M. Lifshitz, *Quantum Mechanics: Non-Relativistic Theory*, 3rd ed. (Butterworth-Heinemann, Singapore, 1981).

[38] B. HuP, J. Liu, and S.-g. Chen, Phys. Lett. A **236**, 533 (1997).